DOI: 10.1002/((please add manuscript number))

Article type: Full paper

Conversion-Type MnO Nanorods as Surprisingly Stable Anode Framework for Sodium-Ion Batteries

Shitong Wang, Yanhao Dong, Fangjun Cao, Yutong Li, Zhongtai Zhang and Zilong Tang**

Dr. S. Wang, Ms. Y. Li, Prof. Z. Zhang, Prof. Z. Tang

State Key Lab of New Ceramics and Fine Processing, School of Materials Science and Engineering, Tsinghua University, Beijing 100084, China

E-mail: tzl@tsinghua.edu.cn

Dr. S. Wang, Dr. Y. Dong

Department of Nuclear Science and Engineering, Massachusetts Institute of Technology, Cambridge, Massachusetts 02139, USA

E-mail: wangst@mit.edu

Dr. F. Cao

College of science, Northwest A&F University, Yangling, Shaanxi 712100, China

Abstract

The emergence of nano materials in the past decades greatly advances modern energy storage devices. Nanomaterials can offer high capacity and fast kinetics yet are prone to rapid morphological evolution and degradation. As a result, they are often hybridized with a stable framework in order to gain stability and fully utilize its advantages. However, candidates of such framework materials are rather limited, with carbon, conductive polymers and Ti-based oxides being the only choices; note these are all inactive or intercalation compounds. Conventionally, alloying-/conversion-type electrodes, which are thought to be electrochemically unstable by themselves, have never been considered as framework materials. In the present work, we shall challenge the above concept. Successful application of conversion-type MnO nanorods as anode framework for high-capacity Mo_2C/MoO_x nanoparticles has been demonstrated in sodium ion batteries (SIBs). Surprisingly, it can stably deliver 110 mAh g^{-1} under extremely high rate of 8,000 mA g^{-1} (~70 C) over 40,000 cycles with no capacity decay. More generally, we consider our work as a proof of concept and expect much more alloying-/conversion-type materials to be explored in such applications.

Lithium-ion batteries (LIBs) and sodium-ion batteries (SIBs) are under rapid development as promising energy storage devices [1]. For anodes, alloying-type (e.g. Si, Sn, Al) and conversion-type materials (e.g. MoO_2, MoS_2, Co_3O_4, and MnO) are attractive because they are able to deliver higher capacities than intercalation materials (e.g. graphite and $Li_4Ti_5O_{12}$) [2]. However, they often suffer from huge volume changes during charge/discharge and have poor cycling stability. A practical way to solve this problem is *via* hierarchical architecture, forming core/shell, yolk/shell, hollow-sphere structures [3] or decorating nanoparticles onto stable three-/two-/one-dimensional (3D/2D/1D) framework [4]. Such hierarchical architectures can benefit from the components at each length scale: large surface area, short diffusion distance and fast kinetics from nano-structures; good wetting and open pore channels from meso-/micro-porous structures; and a stable 3D network that can buffer large volume change and suppress decorated particles from agglomeration/pulverization during cycling [3a, 4].

The most commonly used 3D/2D/1D frameworks are carbon (e.g. nanotubes, graphene and amorphous carbon), conductive polymers [5] and Ti-based oxides (TiO_2 polymorphs, lithium titanates and hydrated lithium titanates) [6], because they experience little volume change during electrochemical charge/discharge and have superior stability over the applicable voltage window. The above fact is also consistent with the properties of intercalation compounds: no significant structural change upon lithiation/delithiation. In comparison, alloying-/conversion-type electrodes have never been considered as good candidates for the framework, because of their poor cycling stability. However, their stability can be greatly improved if one limits the cut-off voltage. For example, there is much less capacity fading in silicon/carbon composite if one limits the voltage window to 0.17~0.6 V vs. Li/Li^+, compared to using 0.05~1.0 V [7]. On the other hand, although not well recognized, switching the application from LIBs to SIBs sometimes helps improve the cycling life of alloying-/conversion-type anodes (meanwhile, capacity is often lowered). For example, MoS_2 anode is

more stable when used in SIBs (>250 cycles) and less in LIBs (<150 cycles) under same current density of 1 A g^{-1} (specific capacity in SIBs is half of that in LIBs) [8]. With the above two considerations and as a proof of concept, in the present study we show successful application of conversion-type MnO nanorods as a stable anode framework hybridized with high-capacity molybdenum oxide and carbide nanoparticles, which can stably deliver 431 mAh g^{-1} at 1000 mA g^{-1} (~2 C) over 600 cycles (43% capacity retention) in LIBs and more surprisingly, 110 mAh g^{-1} at 8000 mA g^{-1} (~70 C) over 40,000 cycles (~100% capacity retention) in SIBs. Previously, MnO was not considered for such applications because in LIBs it has unsatisfactory stability, while in SIBs it has low capacity (less than 200 mAh g^{-1}) and its excellent stability has not been well recognized despite a few reports in the literatures [9].

The synthesis is as follows (see schematics in **Figure 1** and more details in Experimental Section). (1) MnO_y nanorods were first synthesized by hydrothermal method at 160 ^oC for 12 h. (2) MnO_y nanorods were then mixed with ammonium molybdate and dopamine hydrochloride in water/alcohol solution, followed by polymerization using ammonia. The as-obtained precursors (denoted as MnO_y@Mo-PDA hereafter) were washed, collected by centrifuge and dried. (3) The precursors were heat-treated in flowing argon atmosphere at 800 ^oC for 3 h. The final product (denoted as MnO@MOC/C hereafter) is a composite of MnO nanorods, decorated with carbon nanosheets and molybdenum oxide/carbide nanoparticles. As control experiments, we also synthesized (a) composites of carbon nanosheets and molybdenum oxide/carbide nanoparticles (denoted as MOC/C hereafter) by repeating step (2-3) without adding MnO_y nanorods and (b) MnO nanorods (denoted as MnO hereafter) by repeating step (1) and (3) without step (2).

The MnO_y nanorods synthesize in step (1) are about 100 nm in width and several microns in length (**Figure S1**, Supporting Information). After coating step, the precursor MnO_y@Mo-

PDA show uniformly decorations with a porous structure (**Figure S2**, Supporting Information). After heat treatment in argon, the final product MnO@MOC/C show a porous hierarchical structure (**Figures 2a~b**, more images in **Figure S3~S4**, Supporting Information; for specific surface area, see Brunauer-Emmett-Teller (BET) data in **Table S1** and **Figure S5**, Supporting Information), with MnO nanorods (diameter 50~200 nm) coated by ~10 nm thick carbon nanosheets. Energy-dispersive X-ray spectroscopy (EDS) mappings in **Figures 2e~h** confirm uniform distribution of Mn, Mo and O (also see EDS linear scan analysis in **Figure S6**, Supporting Information). Under high-resolution transmission electron microscopy (HRTEM; **Figure 2c**), MnO phase is confirmed with 0.26 nm interlayer spacing (corresponding to (111) crystal plane of MnO, according to JCPDS No. 07-0230). The Mo-containing species are more difficult to characterize directly, probably due to ultrafine sizes and good dispersion in carbon matrix. Selected area electron diffraction (SAED) was therefore conducted in the coating layer (not on MnO nanorods). As shown in the inset of **Figure 2d**, the diffraction patterns circled in orange are associated with (102) lattice plane of Mo_2C (JCPDS No. 71-0242) and dispersed diffraction rings from d=2.0~2.7 Å (half-circled with red dash lines) could be attributed to several molybdenum oxides ((200), (111), ($\bar{2}$11) and ($\bar{2}$02) lattice planes of MoO_2 with d spacing of 2.442, 2.437, 2.426 and 2.403 Å, according to JCPDS No. 32-0671; (100), (002) and (101) lattice planes of MoO_2 with d spacing of 2.459, 2.360 and 2.181 Å, according to JCPDS No. 50-0739; (110) and (102) lattice planes of MoO_3 with d spacing of 2.660 and 2.307 Å, according to JCPDS No. 47-1320).

We next characterized the chemistry for the synthesized materials. We first quantified the chemical composition of MnO@MOC/C by combined inductively coupled plasma mass spectroscopy (ICP-MS; to determine transition metal ratio Mn:Mo) and thermogravimetric analysis (TGA, **Figure S7a**, Supporting Information; to determine carbon content). Assuming

Mn in the form of MnO and Mo in the form of Mo_2C and ignoring the weight change due to oxidation of MnO and Mo_2C, we estimated MnO:Mo_2C:C=6:78:16 by weight (Mn:Mo=1:10 by mole) in the synthesized MnO@MOC/C. Second, the phase of MnO@MOC/C is characterized by XRD in **Figure 3a**, which shows the main phase of face-centered-cubic MnO (JCPDS No. 07-0230) and minor peaks at 34°, 37°, 39°, 52°, 62° and 75° of Mo_2C (JCPDS No. 71-0242) and at around 33° and 48° of Mn_2O_3 (JCPDS No. 24-0508). (The formation of Mn_2O_3 could be due to partial oxidation of MnO.) Third, Raman analysis at the surface of MnO@MOC/C in **Figure 3b** identified the vibration modes of Mn–O (at Raman shift of 640 cm^{-1}) [10], Mo–O (at 125, 151, 192, 249, 295, 345, 416 and 455 cm^{-1}) [11], and Mo–C (at 650 cm^{-1}) [12]. The inset of **Figure 3b** also identified the vibration modes of amorphous carbon (at Raman shift of 1360 cm^{-1}, commonly termed as D peak; amorphous carbon is known to be stable during electrochemical cycling) and graphitized carbon (at 1560 cm^{-1}, commonly termed as G peak; graphitized carbon is known to have high electronic conductivity due to sp^2 bonding). Fourth, the surface chemistry is further analysed by X-ray photoelectron spectroscopy (XPS) in **Figures 3c~f**. For Mo (**Figure 3d**), the peak at 228.8 eV represents Mo–C bond in the form of Mo_2C [13], two peaks at 232.8 and 229.7 eV (associated with Mo(IV) $3d_{3/2}$ and Mo(IV) $3d_{5/2}$) represent Mo–O bond in the form of MoO_2, and two peaks at 235.8 and 232.85 eV (associated with Mo(VI) $3d_{3/2}$ and Mo(VI) $3d_{5/2}$) represent Mo–O bond in the form of MoO_3 [14]. For C (**Figure 3e~f**), bonding states of C–C/C–O, C═O and C–Mo are observed [15]. An interesting observation is the absence of Mn peaks in XPS (absence of Mn 2*p* signals at 630~660 eV in **Figure 3c**). Since XPS is a surface-sensitive (a few nm) technique [16], it indicates full decoration of carbon and molybdenum oxides/carbides on MnO nanorods, which blocks injected electrons from MnO in XPS. Lastly, we conclude the chemical nature of Mo-containing species from the above characterizations. XRD only detected minor Mo_2C phase, much less than MnO phase. But

ICP-MS data suggest a Mn/Mo mole ratio of 1:10. Therefore, most Mo-containing species should be amorphous or very nano in size, which cannot be easily observed by XRD or TEM. This is also consistent with uniform Mo distribution in EDS mapping in **Figure 2g**. Meanwhile, SAED in **Figure 2d** show clear diffraction pattern for Mo_2C, but only weak dispersed diffraction rings for MoO_x-like species. This agrees with the XRD data, indicating Mo_2C should be the main Mo-containing phase, rather than MoO_x. On the other hand, Raman and XPS analysis found stronger Mo–O signals than Mo–C at the surface, which could be due to partial oxidation of Mo_2C at the surface and is consistent with literature reports for molybdenum carbides (e.g. Mo_2C and MoC, whose surface can be easily oxidized) [17].

The synthesized MnO@MOC/C and two control samples (MOC/C and MnO) were tested in a half-cell configuration using Na metal as the reference and counter electrodes for SIBs. (Detailed morphology and structural analysis for the three control samples are listed in **Figures S8~S10**, Supporting Information). MnO@MOC/C and MOC/C both show good rate performance, better than typical carbonaceous and Ti-based anodes for SIBs [18]: When the current density increases from 200 mA g^{-1} to 8000 mA g^{-1}, the discharge specific capacities of MnO@MOC/C decreased from 248.5 to 95.2 mAh g^{-1} (**Figure 4a**; note the anomalously high discharge capacity at the first cycle is due to the formation of solid electrolyte interphase, SEI), and MOC/C's decreased from 273.7 to 124.4 mAh g^{-1} (for MOC/C) (**Figure S11**, Supporting Information). However, the capacities of MnO as well as carbon coated MnO nanorods (denoted as MnO/C hereafter) are unsatisfactory even at relatively low current density (46.9 mAh g^{-1} for MnO and 81.1 mAh g^{-1} for MnO/C at 200 mA g^{-1}), indicating that neither MnO nor carbon are good electrode materials for Na^+ storage in the tested voltage range (0.01 to 3.00 V vs. Na/Na^+**, Figures S12**, Supporting Information). Interestingly, if we estimate the expected value of MnO@MOC/C's capacity from a linear combination of MOC/C's and MnO's, the estimated values are actually lower than the

experimental ones we obtained in **Figure 4a**, especially at small rates. (See **Table S2**, Supporting Information for details.) This demonstrates a synergetic effect of all three components (MnO nanorods, carbon nanosheets and Mo_2C/MoO_x active materials), in boosting the capacity and rate performance. MnO@MOC/C further shows stable cycling with 110 mAh g^{-1} discharge capacity for 40,000 cycles at 8000 mA g^{-1} (~70 C), with little capacity decay and close to 100% Coulomb efficiency (red curve in **Figure 4b**). In comparison, even though the control samples MnO (black curve in **Figure 4b**) and MnO/C also show stable cycling, their capacities are too low to be considered useful (consistent with literature reports [9]), which is not useful in any sense. This is apparently the reason why pure MnO had never been considered as a good candidate in SIBs. On the other hand, MOC/C suffers from poor cyclability, whose discharge capacity decreases from 159 to ~0 mAh g^{-1} after 3500 cycles at 8000 mA g^{-1} (blue curve in **Figure 4b**). The carbon content of MOC/C is estimated to be 42 wt% by TGA (**Figure S7b**, Supporting Information), which is higher than that of MnO@MOC/C (16 wt%). So carbon alone cannot completely explain the superior cycling stability of MnO@MOC/C and the poor cycling stability of MOC/C highlights the critical role of MnO nanorods, which provides a rigid framework to suppress agglomeration and coarsening of carbon nanosheets and Mo_2C/MoO_x nanoparticles. To confirm the microstructure stability of MnO@MOC/C, the electrode materials after 40,000 cycles were investigated under TEM and showed well maintained morphology (of carbon-decorated MnO nanorods, in **Figure 4c**). Therefore, the superior electrochemical and microstructural stability demonstrates another synergetic effect from the design of such a hierarchical architecture: MnO as a rigid framework, Mo_2C/MoO_x offering high capacity and probably carbon buffering stress/strain.

As a further proof of the superior electrochemical properties, we assembled full cells using MnO@MOC/C as anodes and $Na_3V_2(PO_4)_3$ as cathodes. **Figure 4d** illustrates the voltage-to-capacity curves of the full cell at various current densities. With the increasing of current densities from 100 mA g^{-1} to 2000 mA g^{-1} (for each 8 cycles), the discharge specific capacity decreased from 204.8 mAh g^{-1} to 48.9 mAh g^{-1}. Due to the irreversible reactions in both cathode and anode together with limited sodium ions in full cells compared with massive Na^+ in half cells, the columbic efficiency (CE) is not as good as that in half cells, especially for the first few cycles (only 60%). However, the CE increases to ＞90% after 20 cycles. After the rate performances test, the electrochemical reactions became reversible and showed stable cycling at relatively high current density of 500 mA g^{-1} for the next 150 cycles with capacity retention of ~60% (**Figure S13**, Supporting Information). The results demonstrate the rapid electrochemical kinetics of MnO@MOC/C as an anode for SIBs (**Figure 4e**), but also emphasize the significance of CE in the practical full cells. More efforts should be made to decrease the side reactions in both anodes and cathodes to meet the requirements of real-life SIBs applications.

To understand the reaction mechanism better, we conducted cyclic voltammetry (CV) measurements (from 0.01 V to 3.00 V vs. Na/Na^+ at a scan rate of 0.1 mV s^{-1}; results shown in **Figure 5a**) for MnO@MOC/C. In the first cycle of discharge (from 3.00 V to 0.01 V with a negative current), much cathodic reaction takes place below 1.6 V. This is not seen in subsequent cycles and is attributed to the formation of SEI [3d, 6g, h, 9a]. After the first cycle of discharge, CV curves are mostly unchanged, suggesting a stable redox behaviour. Interestingly, the CV curves are flat and diffusive, except small redox peaks at ~1.6 V during discharge (probably MoO_x reduction to Na_yMoO_x) [19], at ~1.7 V during charge (probably Na_yMoO_x oxidation to MoO_x), and at ~2.3 V during charge (probably Mn oxidation) [20]. Such diffusive CV curves could come from pseudocapacitive behaviour, or defects/disorders

(i.e. a distribution of redox potentials due to a large amount of surface/lattice defects) [21]. It is further supported by analysing peak current density j_p vs. scan rate v in a log-log plot (**Figure S14**, Supporting Information), giving a b value of 0.99 for MnO@MOC/C (b value is 1.0 for purely surface-controlled process, i.e. a capacitor-like behaviour; and 0.5 for purely diffusion-controlled process, i.e. a battery-like behaviour) [22]. In comparison, b value of control samples is 1.0 for MOC/C and 0.45 for MnO (**Figure 5b**). The transition from more diffusion-controlled process to more surface-controlled one may improve the cycling stability of conversion-type Mo_2C/MoO_x—which contributes most capacity in MnO@MOC/C—especially at high rates. This effect is known in $LiFePO_4$ as cathode in LIBs: nano $LiFePO_4$ at slow charge/discharge rates or micro $LiFePO_4$ show two-phase behavior and are prone to degradation, while nano $LiFePO_4$ at fast rates show solid-solution behavior and have excellent cycling stability [23].

The above b-value analysis also suggests diffusion is likely less a problem in our MnO@MOC/C, which offers much better kinetics and hence rate performance than bulk Mo_2C/MoO_x [24]. To further demonstrate this, we conducted galvanostatic intermittent titration technique (GITT, **Figure 5c**) and calculated the apparent diffusion coefficient D_{Na} according to [25]

$$D_{Na} = \frac{4}{\pi}\left(\frac{V_M}{AFZ_i}\right)^2\left[I_0\left(\frac{dE}{d\delta}\right)\Big/\left(\frac{dE}{d\sqrt{t}}\right)\right]^2, t << \frac{L^2}{D_{Na}} \quad (1)$$

where V_M is molar volume of active material (here we use 22 cm^3 mol^{-1} of Mo_2C for simplification), A is total contact area between electrolyte and electrodes, F is Faraday constant, I_0 is applied constant electric current, Z_i is valence of species, $dE/d\delta$ is determined from initial stoichiometry, L is the thickness of electrode, E is electrode voltage, δ is the deviation from the stoichiometric ratio, and t is the time during constant current pulse. The

obtained apparent diffusivity coefficient D_{Na} (**Figure 5d**) is surprisingly high, in the range of 10^{-12}~10^{-10} cm^2 s^{-1}, which are higher than typical high-rate LIB electrodes such as $LiFePO_4$ (10^{-18}~10^{-12} cm^2 s^{-1}) [26] and $Li_4Ti_5O_{12}$ (10^{-16}~10^{-13} cm^2 s^{-1}) [27], and comparable to typical high-rate SIB electrode P2-$Na_{2/3}[Ni_{1/3}Mn_{2/3}]O_2$ (10^{-10}~10^{-9} cm^2 s^{-1}) [28]. (The above diffusivity data are all calculated from GITT measurements.) A closer inspection on the GITT curve and D_{Na} also suggests a relatively poor kinetics at the end of charge (2.0~3.0 V vs. Na/Na^+, **Figure S15**, Supporting Information). It may be because higher-valence electronically-insulating Mo^{6+} forms at such voltages, imposing a kinetic issue for electron transport. This problem may be solved by transitional metal doping (e.g. Co-N doping [29]) of as-synthesized Mo_2C/MoO_x nanoparticles, which should improve our materials further. Also note in the GITT data is that the overpotential of MnO@MOC/C increases at higher voltage in the desodiation process (similar trend also holds in LIBs; see **Figure S16**, Supporting Information). This could be due to two reasons. First, at higher voltages, Mo ions are oxidized to higher valence so the electronic conductivity may become worse, which increases the overpotential. Second, Li^+ diffusion in MoO_x and Mo_2C should follow an interstitial mechanism. So at higher voltages, the concentration of charge carriers (lithium interstitial) becomes lower, which also increases the overpotential.

The three electrode materials (MnO@MOC/C, MOC/C and MnO) were further tested in LIBs, in a half-cell configuration using Li metal as the reference and counter electrode. The voltage-to-capacity curves at the current density of 50 mA g^{-1} are shown in **Figure 6a**, with 888.3 mAh g^{-1} for MnO@MOC/C, 992.4 mAh g^{-1} for MOC/C and 679.3 mAh g^{-1} for MnO. Compared with the smooth curves of MnO@MOC/C and MOC/C with apparent plateaus, MnO showed a plateau at ~0.6 V during lithiation, indicating a Faradaic two-phase transformation process. MnO@MOC/C has a good rate performance, with discharge capacity decreased from 888.3 to 508.3 mAh g^{-1} when the current density increased from 50 to 2000

mA g^{-1} (**Figure 6b** and **Figure S17**, Supporting Information). In comparison, the specific capacity of the MOC/C decreased much faster from 985.8 to 354.7 mA g^{-1} (MOC/C) and MnO's decreased from 643.8 to 375.6 mA g^{-1} when the current density increased from 50 to 2000 mA g^{-1}. The capacity and rate performance of MnO@MOC/C in LIBs is highly competitive with MnO-, Mo_2C- or MoO_x-based anodes reported in literature references (**Table S3**, Supporting Information). However, few of MnO@MOC/C, MOC/C and MnO show good stability in prolonged cycling of >1300 cycles (**Figure 6c**) in LIBs, which is different from the stable cycling of MnO@MOC/C in SIBs. (See comparison with recently reported MnO-, Mo_2C- and MoO_x-based anodes in SIBs references in **Table S4**, Supporting Information). The reason could be due to much larger capacity of MnO in LIBs (as shown in **Figure 4** and **Figure 6)**, resulting in large volume change and serious pulverization of the hybrid materials. TEM of MnO@MOC/C after 500 cycles in LIBs (**Figure S18**, Supporting Information) also shows thicker SEI than that after 40,000 cycles in SIBs (see **Figure 4c** for comparison). Therefore, limiting the capacity (hence less volume change and higher stability) of conversion-type anodes is important when using them as the framework in hybrid architectures.

To summarize, we designed and synthesized 1D@2D/0D hierarchical architectures with 1D MnO nanorods, 2D carbon nanosheets and 0D Mo_2C/MoO_x nanoparticles. Our work demonstrated successful application of conversion-type MnO nanorods as super-stable anode frameworks in SIBs. It can stably deliver ~110 mAh g^{-1} at ~70 C over 40,000 cycles with no apparent capacity decay. Our work suggests that conversion reaction is not inherently related to fast degradation. If one limits the capacity in use (e.g. switching the application of MnO from LIBs to SIBs as in the present work), conversion-type materials may also be potentially useful as a stable framework. We believe this to be a general strategy applicable to many conversion-/alloying-type electrode materials and it provides new opportunities to explore the

synthesis and to tune the interfacial/bonding characteristics between the host framework and the loaded high-capacity nano materials.

Experimental Section

Materials synthesis. *Synthesis of MnO_y nanorods.* 90 mg $KMnO_4$ and 27 mg of polyvinylpyrrolidone (PVP) were dissolved in 30 mL of deionized (DI) water under vigorous magnetic for 10 min, forming a homogeneous solution in purple. The solution was next transferred into a 50 mL Teflon-lined stainless-steel autoclave, sealed and maintained at 170 ^{o}C for 12 h for a hydrothermal reaction. After hydrothermal reaction, the precipitates were collected and washed with DI water and ethanol for several times.

Synthesis of MnO@MOC/C, MOC/C, MnO and MnO/C. For the synthesis of MnO@MOC/C, 8 mg as-synthesized MnO_y nanorods were dispersed into 12 mL deionized water with ultrasonic treatment to form a suspension, followed by addition of 24 mg ammonium molybdate ($(NH_4)_6Mo_7O_{24}\cdot 4H_2O$), 8 mg dopamine hydrochloride and 8 mL ethanol under intense stirring. 20 μL ammonium hydroxide (25~28 wt% ammonia in water) was next added into the above suspension, followed by intense stirring for 6 h. The collected materials were dried and heated at 800 ^{o}C in flowing argon for 3 h with a heating rate of 5 ^{o}C min^{-1} to obtain the final product MnO@MOC/C. For the synthesis of reference sample MOC/C, 24 mg ammonium molybdate and 8 mg dopamine hydrochloride were added into 8 mL ethanol under intense stirring. 20 μL ammonium hydroxide (25~28 wt% ammonia in water) was next added into the above suspension, followed by intense stirring for 6 h. The collected materials were dried and heated at 800 ^{o}C in flowing argon for 3 h with a heating rate of 5 ^{o}C min^{-1} to obtain the final product MOC/C. For the synthesis of reference sample MnO nanorods, the as-synthesized MnO_y nanorods was heated at 800 ^{o}C in flowing argon for 3 h with a heating rate of 5 ^{o}C min^{-1} to obtain the final product MnO. For the synthesis of reference sample carbon coated MnO nanorods

MnO/C, 8 mg as-synthesized MnO_y nanorods were dispersed into 12 mL deionized water with ultrasonic treatment to form a suspension, followed by addition of 8 mg dopamine hydrochloride and 8 mL ethanol under intense stirring. 20 µL ammonium hydroxide (25~28 wt% ammonia in water) was next added into the above suspension, followed by intense stirring for 6 h. The collected materials were dried and heated at 800 ^{o}C in flowing argon for 3 h with a heating rate of 5 ^{o}C min^{-1} to obtain the final product MnO/C.

Synthesis of $Na_3V_2(PO_4)_3$ cathode. $Na_3V_2(PO_4)_3$ materials was synthesized by hydrothermal reactions of V_2O_5, $H_2C_2O_4{\cdot}2H_2O$ and NaH_2PO_4 followed by glucose carbon coating process, with details described previously[30].

Characterizations. Scanning electron microscope (SEM, MERLIN VP Compact), transmission electron microscopy (TEM, Hitachi-HT7700), high resolution TEM (HRTEM, JEM-2100F) and scanning TEM (STEM, JEM-2100F) were used to analyze the morphology and structures. X-ray diffraction (XRD, Rigaku D/Max-B X; Cu Kα radiation λ=1.5418 Å) was used to identify the phase. Raman spectrometer (HR800, HORIBA; 633 nm line of helium-neon beam) was used for Raman spectrum analysis. X-ray photoelectron spectroscopy (XPS, Escalab 250XI system, Thermo Fisher Scientific) was used to analyze surface chemistry. Transition metal ratios were obtained from inductively coupled plasma mass spectroscopy (ICP-MS, Thermo Fisher Scientific). TGA analysis was conducted on thermogravimetric analyzer (STA 449F3) instrument in flowing air at 5 °C min^{-1} ramping rate from 50 to 600 °C. Brunauer-Emmett-Teller (BET) measurements (Autosorb-iQ2-MP, Quanta Chrome) were used to calculate specific surface areas.

Electrochemical measurements. To prepare the electrode composite, 70 wt% active materials, 20 wt% Super P, and 10 wt% poly(vinylidene fluoride) binder were mixed in N-methyl-2-pyrrolidinone (NMP). The obtained slurry was casted on Cu (for MnO@MOC/C, MOC/C, MnO/C and MnO anodes) or Al foil (for $Na_3V_2(PO_4)_3$ cathodes) and dried at 110 °C under vacuum overnight. For half-cell tests, lithium and sodium metal was used as the counter and reference electrodes in SIBs and LIBs,

respectively. For full-cell tests in SIBs, $Na_3V_2(PO_4)_3$ was used as the cathode and MnO@MOC/C was used as the anode. Glass fibers (Whatman Inc.) and microporous membranes (Celgard 2400) were used as separators in SIBs and LIBs, respectively. Ethylene carbonate-dimethyl carbonate (1:1 in volume) with 1 M $NaClO_4$ and 5 wt % fluoroethylene carbonate additive and ethylene carbonate-dimethyl carbonate (1:1 in volume) with 1.0 M $LiPF_6$ were used as electrolytes in SIBs and LIBs, respectively. Mass loading of all anode samples is about 1.0 mg cm^{-2}. Mass loading of $Na_3V_2(PO_4)_3$ cathodes is about 4.5 mg cm^{-2}, providing ~50% excessive area-capacity compared with MnO@MOC/C anodes. Cyclic voltammetry (CV) were performed using IM6 (Bas-Zahner) electrochemical workstation. Galvanostatic intermittent titration technique (GITT) measurements were conducted at 50 mA g^{-1} with a duration of 40 min, followed by 20 h's relaxation. GITT data were obtained in cell coins after 5 cycles at 100 mA g^{-1}. All half-/full-cell tests were conducted using LAND 2001A Cell test system between 0.05~3.00 V (for half cells) and 0.05~4.00 V (for full cells) at ambient temperature.

References

[1] B. Dunn, H. Kamath and J. M. Tarascon, *Science* **2011**, *334*, 928.

[2] a) V. Aravindan, Y. S. Lee and S. Madhavi, *Adv. Energy Mater.* **2015**, *5*, 1402225; b) L. Jiang, Z. Wu, Y. Wang, W. Tian, Z. Yi, C. Cai, Y. Jiang and L. Hu, *ACS Nano* **2019**, *13*, 10376; c) Y. Wang, Z. Wu, L. Jiang, W. Tian, C. Zhang, C. Cai and L. Hu, *Nanoscale Adv.* **2019**, *1*, 4365.

[3] a) J. Mei, T. Liao, L. Kou and Z. Sun, *Adv. Mater.* **2017**, *29*, 1700176; b) Z. Wang, L. Zhou and X. W. David Lou, *Adv. Mater.* **2012**, *24*, 1903; c) J. Cui, S. Yao and J.-K. Kim, *Energy Stor. Mater.* **2017**, *7*, 64; d) Y. Yang, M. Luo, Y. Xing, S. Wang, W. Zhang, F. Lv, Y. Li, Y. Zhang, W. Wang and S. Guo, *Adv. Mater.* **2018**, 1706085; e) W.-M. Chen, L. Qie, Y. Shen, Y.-M. Sun, L.-X. Yuan, X.-L. Hu, W.-X. Zhang and Y.-H. Huang, *Nano Energy* **2013**, *2*, 412.

[4] Q. Wei, F. Xiong, S. Tan, L. Huang, E. H. Lan, B. Dunn and L. Mai, *Adv. Mater.* **2017**, *29*, 1602300.

[5] M. Zheng, H. Tang, L. Li, Q. Hu, L. Zhang, H. Xue and H. Pang, *Adv Sci (Weinh)* **2018**, *5*, 1700592.

[6] a) S. Wang, W. Quan, Z. Zhu, Y. Yang, Q. Liu, Y. Ren, X. Zhang, R. Xu, Y. Hong, Z. Zhang, K. Amine, Z. Tang, J. Lu and J. Li, *Nat. Commun.* **2017**, *8*, 627; b) W. Zhou, H. Liu, R. I. Boughton, G. Du, J. Lin, J. Wang and D. Liu, *J. Mater. Chem.* **2010**, *20*, 5993; c) Z. Hong and M. Wei, *J. Mater. Chem. A* **2013**, *1*, 4403; d) S. Wang, Y. Yang, W. Quan, Y. Hong, Z. Zhang, Z. Tang and J. Li, *Nano Energy* **2017**, *32*, 294; e) L. Zhao, S. Wang, F. Pan, Z. Tang, Z. Zhang, S. Zhong and J. Zhang, *J. Mater. Chem. A* **2018**, *6*, 11688; f) S. Wang, Y. Yang, C. Jiang, Y. Hong, W. Quan, Z. Zhang and Z. Tang, *J. Mater. Chem. A* **2016**, *4*, 12714; g) S. Wang, Z. Zhang, Y. Yang and Z. Tang, *ACS Appl. Mater. Interfaces* **2017**, *9*, 23741; h) Y. Yang, S. Wang, M. Luo, W. Wang, F. Lv, Z. Tang and S. Guo, *J. Mater. Chem. A* **2017**, *5*, 12096; i) Y. Yang, S. Wang, S. Lin, Y. Li, W. Zhang, Y. Chao, M. Luo, Y. Xing, K. Wang, C. Yang, P. Zhou, Y. Zhang, Z. Tang and S. Guo, *Small Methods* **2018**, 1800119; j) Y. N. Mei, Y. H. Huang and X. L. Hu, *J. Mater. Chem. A* **2016**, *4*, 12001; k) S. Wang, F. Cao, Y. Li, Z. Zhang, D. Zhou, Y. Yang and Z. Tang, *Adv. Sci.* **2019**, 1900028; l) S. Wang, Y. Yang, Y. Dong, Z. Zhang and Z. Tang, *J. Adv. Ceram.* **2019**, *8*, 1; m) X. Liu, L. Zhao, S. Wang, M. Chao, Y. Li, J. Leng, J. Zhang and Z. Tang, *Sci Bull* **2019**, *64*, 1148.

[7] L. Hu, H. Wu, Y. Gao, A. Cao, H. Li, J. McDough, X. Xie, M. Zhou and Y. Cui, *Adv. Energy Mater.* **2011**, *1*, 523.

[8] G. Wang, J. Zhang, S. Yang, F. Wang, X. Zhuang, K. Müllen and X. Feng, *Adv. Energy Mater.* **2017**, *8*, 1702254.

[9] a) Y. He, P. Xu, B. Zhang, Y. Du, B. Song, X. Han and H. Peng, *ACS Appl. Mater. Interfaces* **2017**, *9*, 38401; b) X. Zhang, G. Zhu, D. Yan, T. Lu and L. Pan, *J. Alloys Compd.* **2017**, *710*, 575.

[10] a) L. Sheng, H. Jiang, S. Liu, M. Chen, T. Wei and Z. Fan, *J. Power Sources* **2018**, *397*, 325; b) Y.-F. Han, K. Ramesh, L. Chen, E. Widjaja, S. Chilukoti and F. Chen, *J. Phys. Chem. C* **2007**, *111*, 2830; c) A. Ramírez, P. Hillebrand, D. Stellmach, M. M. May, P. Bogdanoff and S. Fiechter, *J. Phys. Chem. C* **2014**, *118*, 14073.

[11] M. A. Camacho-López, L. Escobar-Alarcón, M. Picquart, R. Arroyo, G. Córdoba and E. Haro-Poniatowski, *Opt. Mater.* **2011**, *33*, 480.

[12] a) M. Liu, Y. Yang, X. Luan, X. Dai, X. Zhang, J. Yong, H. Qiao, H. Zhao, W. Song and X. Huang, *ACS Sustain. Chem. Eng.* **2018**, *6*, 14356; b) D. Geng, X. Zhao, Z. Chen, W. Sun, W. Fu, J. Chen, W. Liu, W. Zhou and K. P. Loh, *Adv. Mater.* **2017**, *29*, 1700072.

[13] Y. Lu, H. Ang, Q. Yan and E. Fong, *Chem. Mater.* **2016**, *28*, 5743.

[14] Y. Sun, X. Hu, W. Luo and Y. Huang, *ACS Nano* **2011**, *5*, 7100.

[15] Y. Zhu, S. Wang, Y. Zhong, R. Cai, L. Li and Z. Shao, *J. Power Sources* **2016**, *307*, 552.

[16] a) S. Xuan, W. Jiang, X. Gong, Y. Hu and Z. Chen, *J. Phys. Chem. C* **2008**, *113*, 553; b) H. Wang, X. Fei, L. Wang, Y. Li, S. Xu, M. Sun, L. Sun, C. Zhang, Y. Li, Q. Yang and Y. Wei, *New J. Chem.* **2011**, *35*, 1795.

[17] a) L. Yang, X. Li, S. He, G. Du, X. Yu, J. Liu, Q. Gao, R. Hu and M. Zhu, *J. Mater. Chem. A* **2016**, *4*, 10842; b) F. Lyu, S. Zeng, Z. Sun, N. Qin, L. Cao, Z. Wang, Z. Jia, S. Wu, F. X. Ma, M. Li, W. Wang, Y. Y. Li, J. Lu and Z. Lu, *Small* **2019**, *15*, 1805022; c) B. Yu, D. Yang, Y. Hu, J. He, Y. Chen and W. He, *Small Methods* **2019**, *3*, 1800287; d) H. Lin, Z. Shi, S. He, X. Yu, S. Wang, Q. Gao and Y. Tang, *Chem Sci* **2016**, *7*, 3399.

[18] L. Li, Y. Zheng, S. Zhang, J. Yang, Z. Shao and Z. Guo, *Energy Environ. Sci.* **2018**, *11*, 2310.

[19] a) J. Jiang, W. Yang, H. Wang, Y. Zhao, J. Guo, J. Zhao, M. Beidaghi and L. Gao, *Electrochim. Acta* **2017**, *240*, 379; b) L. Yang, X. Li, Y. Ouyang, Q. Gao, L. Ouyang, R. Hu, J. Liu and M. Zhu, *ACS Appl. Mater. Interfaces* **2016**, *8*, 19987.

[20] Y. Chu, L. Guo, B. Xi, Z. Feng, F. Wu, Y. Lin, J. Liu, D. Sun, J. Feng, Y. Qian and S. Xiong, *Adv. Mater.* **2018**, *30*, 1704244.

[21] H. S. Kim, J. B. Cook, H. Lin, J. S. Ko, S. H. Tolbert, V. Ozolins and B. Dunn, *Nat. Mater.* **2017**, *16*, 454.

[22] V. Augustyn, J. Come, M. A. Lowe, J. W. Kim, P. L. Taberna, S. H. Tolbert, H. D. Abruna, P. Simon and B. Dunn, *Nat. Mater.* **2013**, *12*, 518.

[23] J. Lim, Y. Li, D. H. Alsem, H. So, S. C. Lee, P. Bai, D. A. Cogswell, X. Liu, N. Jin, Y. S. Yu, N. J. Salmon, D. A. Shapiro, M. Z. Bazant, T. Tyliszczak and W. C. Chueh, *Science* **2016**, *353*, 566.

[24] H. S. Kim, J. B. Cook, S. H. Tolbert and B. Dunn, *J. Electrochem. Soc.* **2015**, *162*, A5083.

[25] a) W. Weppner, *J. Electrochem. Soc.* **1977**, *124*, 1569; b) Y. Li, S. Wang, Y. Dong, Y. Yang, Z. Zhang and Z. Tang, *Adv. Energy Mater.* **2019**, *10*, 1903411.

[26] a) K. Tang, X. Yu, J. Sun, H. Li and X. Huang, *Electrochim. Acta* **2011**, *56*, 4869; b) Y. Zhu and C. Wang, *J. Phys. Chem. C* **2010**, *114*, 2830.

[27] a) X. Hao and B. M. Bartlett, *Adv. Energy Mater.* **2013**, *3*, 753; b) F. Wunde, F. Berkemeier and G. Schmitz, *J. Power Sources* **2012**, *215*, 109.

[28] D. H. Lee, J. Xu and Y. S. Meng, *Phys. Chem. Chem. Phys.* **2013**, *15*, 3304.

[29] L. Yang, J. Yu, Z. Wei, G. Li, L. Cao, W. Zhou and S. Chen, *Nano Energy* **2017**, *41*, 772.

[30] W. Ren, Z. Zheng, C. Xu, C. Niu, Q. Wei, Q. An, K. Zhao, M. Yan, M. Qin and L. Mai, *Nano Energy* **2016**, *25*, 145.

Supporting Information

Supporting Information is available from the Wiley Online Library or from the author.

Acknowledgements

S Wang, Y Dong and F Cao contributed equally to this work. This study was financially supported by the National Natural Science Foundation of China (No. 51772163).

Received: ((will be filled in by the editorial staff))

Revised: ((will be filled in by the editorial staff))

Published online: ((will be filled in by the editorial staff))

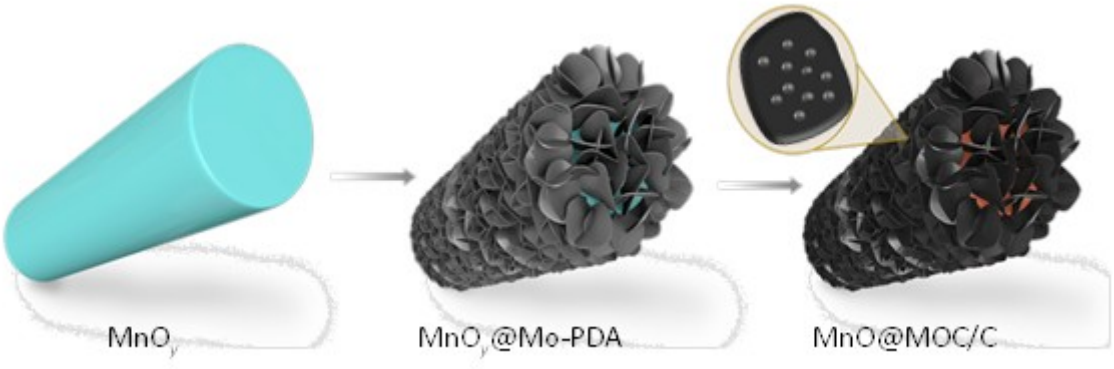

Figure 1. Schematics for material synthesis of MnO@MOC/C hybrid.

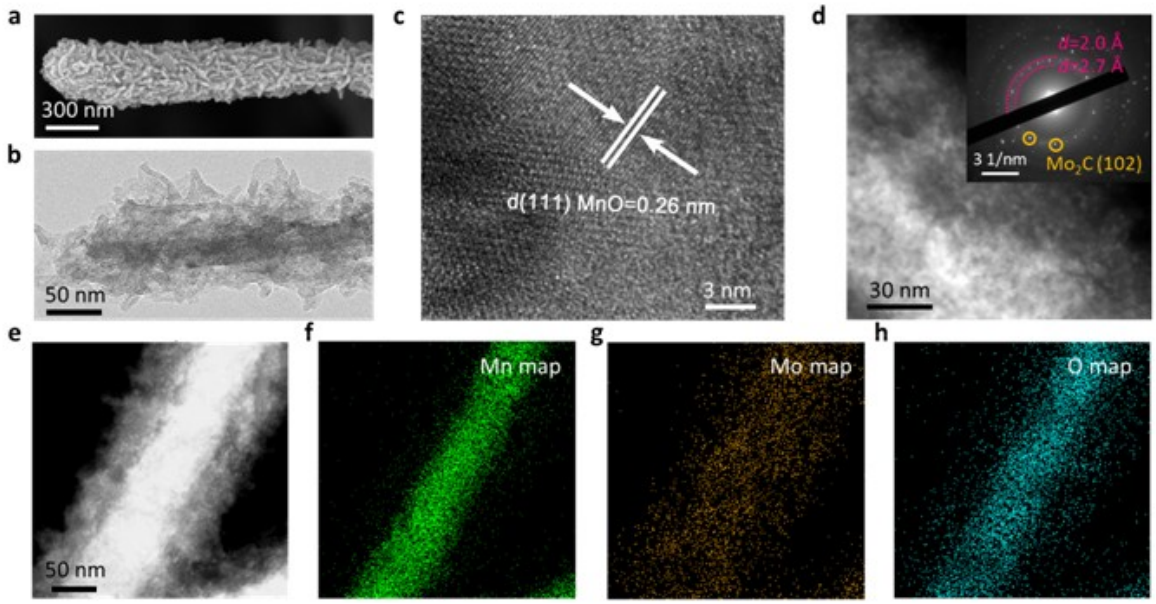

Figure 2. Morphology of MnO@MOC/C hybrid. (a) SEM, (b, c) HRTEM, (d) STEM (inset: SAED analysis of the 2D carbon area), (e) HRTEM images and EDS mapping of (f) Mn, (g) Mo and (h) O elements.

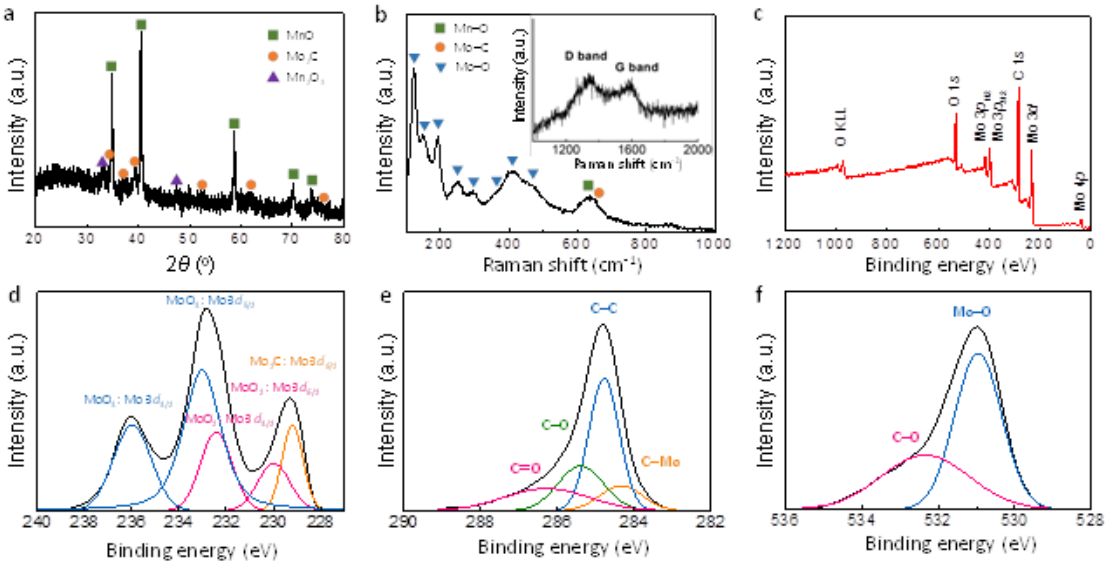

Figure 3. Characterizations of MnO@MOC/C. (a) XRD, (b) Raman, and (c) XPS spectrum. Inset of (b): high frequency Raman data for C–C vibrations. Also shown are fitting results for (d) Mo 3*d*, (e) C 1*s* and (f) O 1*s* peaks from XPS.

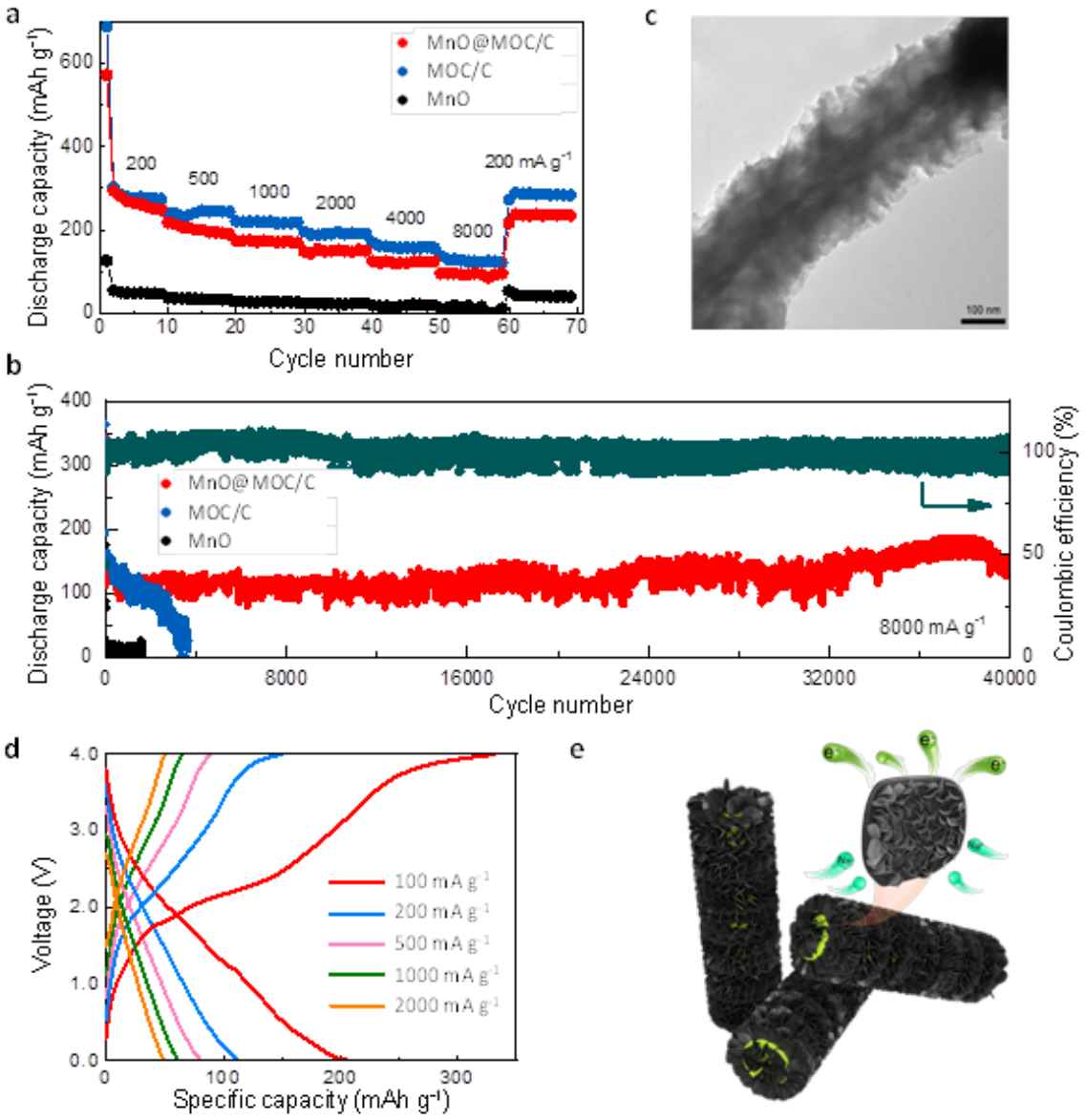

Figure 4. Electrochemical analysis of MnO@MOC/C hybrid in SIBs. (a) Rate and (b) cycling performances at 8000 mA g^{-1} of MnO@MOC/C, MOC/C and MnO electrodes. (c) TEM of MnO@MOC/C after 40,000 cycles. (d) Galvanostatic discharge/charge profiles from 100 to 2000 mA g^{-1} of full-cell using MnO@MOC/C as the anode and $Na_3V_2(PO_4)_3$ as the cathode in SIBs. (e) Schematic diagram of the fast Na^+ transfer behaviors of MnO@MOC/C in SIBs.

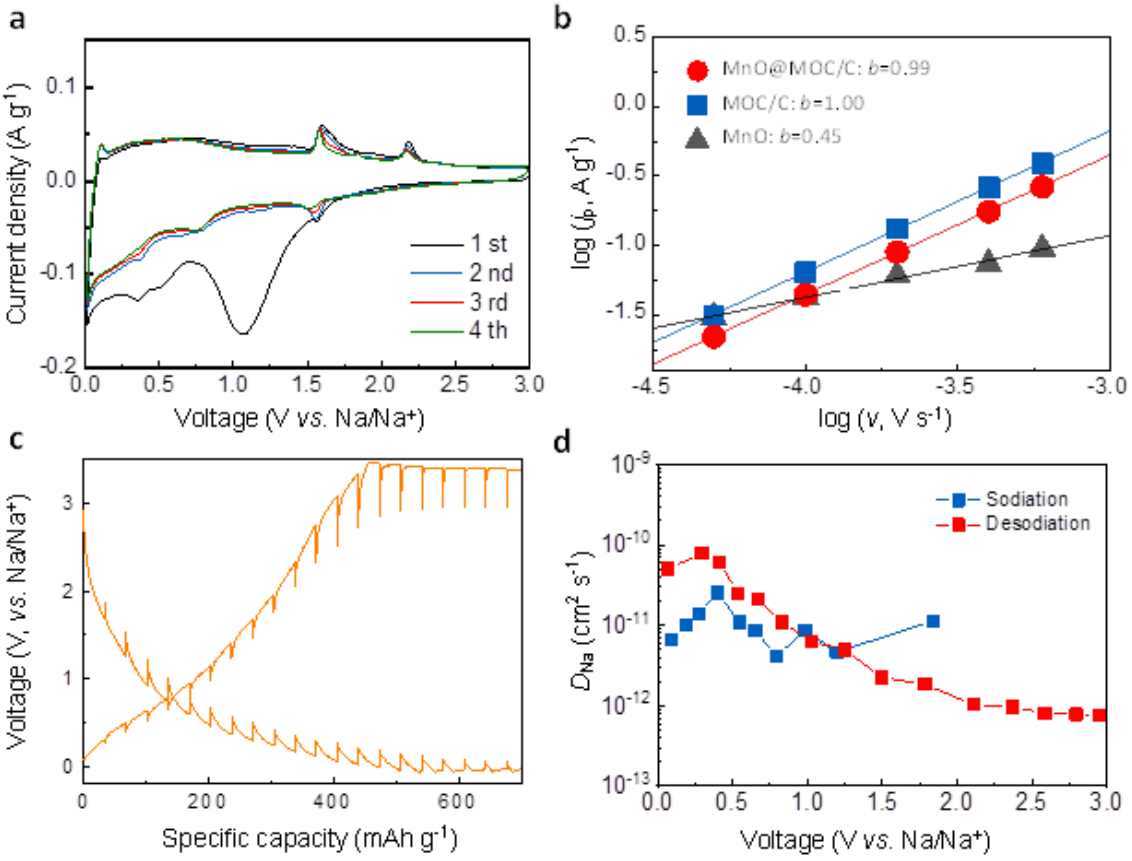

Figure 5. Electrochemical mechanism of MnO@MOC/C hybrid in SIBs. (a) CV curves at 0.1 mV s^{-1} (b) *b*-values analysis and (c) GITT of MnO@MOC/C. (d) Na^+ diffusion coefficient (D_{Na}) calculated from GITT.

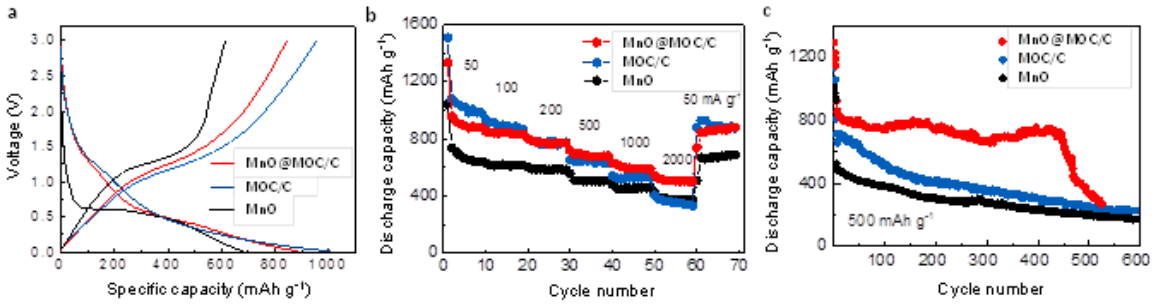

Figure 6. Electrochemical analysis of MnO@MOC/C hybrid in LIBs. (a) Galvanostatic discharge/charge profiles at 50 mA g^{-1}, (b) rate performances, and (c) cycling performances at 500 mA g^{-1} of MnO@MOC/C, MOC/C and MnO electrodes.

We demonstrate successful application of conversion-type MnO nanorods as super-stable anode framework for high-capacity nano Mo_2C/MoO_x in sodium-ion batteries. This work challenges conventional consensus that conversion-/alloying-type electrode materials cannot be used as stable hosts and opens up a new door to the designing of hierarchical architectures.

Conversion-Type MnO Nanorods as Surprisingly Stable Anode Framework for Sodium-Ion Batteries

Key words: Sodium-ion battery, Lithium-ion battery, Nano materials, MnO, Molybdenum

TOC figure